JPE 18-2-13

https://doi.org/10.6113/JPE.2018.18.2.456
ISSN(Print): 1598-2092 / ISSN(Online): 2093-4718

Development and Testing of a 10 kV 1.5 kA Mobile DC De-Icer based on Modular Multilevel Converter with STATCOM Function

Pengfei Hu[†], Yiqiao Liang[**], Yi Du[***], Renming Bi[**], Chonglin Rao[**], and Yang Han[*]

[†,*]School of Mechanical and Electrical Engineering, University of Electronic Science and Technology of China, Chengdu, China
[**]Zhejiang Guirong Xieping Technology Co., Ltd., Hangzhou, China
[***]Power Economic Research Institute of State Grid Fujian Electric Power Company, Fuzhou, China

Abstract

This paper introduces the development of a de-icer based on a full-bridge modular multilevel converter (FMMC). The FMMC can generate a wide range of DC voltages owing to its modularity, scalability, and redundancy, which makes it suitable for ice-melting applications. First, operating principles and voltage ranges are analyzed when FMMC is applied as a mobile de-icer. Second, two new startup strategies, constant modulation index and constant power startup strategies, are proposed. Third, the main control strategies of the de-icer are proposed. Fourth, a novel rated-current zero-power test scheme is proposed to simplify test conditions. Finally, a 10 kV 1.5 kA mobile MMC de-icer is designed and built, and experiments are carried out to validate the proposed startup, control strategies, and rated-current zero-power test scheme.

Key words: Control strategy, DC de-icer, Experimental test, Modular multilevel converter, Rated-current zero-power test, Startup strategy

I. INTRODUCTION

Ice accumulation on overhead transmission lines is one of the potential risks that may lead to power transmission interruption. In January 1998, a series of severe ice storms affected much of Eastern Canada and Northeastern USA. The ice accumulation on transmission lines caused almost 900 km of transmission line collapse [1]. In 2008, an unexpected ice disaster happened throughout South China, where 36,740 overhead transmission lines, 2018 substations, and more than 8000 towers with powers ranging from 110 kV to 500 kV were destroyed [2]. Hundreds of cities were subjected to blackout and billions of wealth were lost [3]. The severity of ice disasters has promoted many studies into techniques that aim to mitigate a possible recurrence. Four kinds of methods are mainly proposed to deal with this issue. Building a strong grid is one method. Three different principles (mechanical, chemical, and thermal principles) to remove the ice comprise the other three methods [4]. Of these four methods, using the Joule heat produced by a large current to melt ice is the most efficient and environmentally friendly method. Theoretically, AC and DC currents can be used to melt the ice. However, an AC de-icer has the disadvantage of large capacity due to the large inductance of a high-voltage overhead transmission line. Different kinds of AC/DC rectifiers can be employed to generate a DC current. The most widely employed rectifier is the line-commutated converter (LCC) based on thyristors [5], [6]. Although the LCC technology is mature, many drawbacks are still present. This technology requires a large transformer and harmonic filters, which occupy a large area. Moreover, it is almost only used as a stationary-type de-icer due to its large volume, which can only melt ice for the

Manuscript received May 25, 2017; accepted Nov. 18, 2017
Recommended for publication by Associate Editor Yun Zhang.
[†]Corresponding Author: pfhu@uestc.edu.cn
Tel: +86-13658095156, Univ. Electron. Sci. Tech. China
[*]School of Mechanical and Electrical Engineering, University of Electronic Science and Technology of China, China
[**]Zhejiang Guirong Xieping Technology Co., Ltd., China
[***]Power Economic Research Institute of State Grid Fujian Electric Power Company, China

transmission lines connected to the substation where the stationary de-icer is installed. Considering the large amounts of 110 and 220 kV overhead transmission lines in China, building one stationary-type de-icer for each substation is costly. Hence, a mobile de-icer with wide ice-melting current range is the best option.

Voltage-source converters (VSCs) that can be employed to convert AC to DC have many types. Among them, the two-level converter, diode-clamped multilevel converter, flying capacitor multilevel converter, and modular multilevel converter (MMC) are the most studied ones. MMC has drawn increasing interests from scholars and power engineers in medium- and high-voltage high-power applications, such as high-voltage direct-current (HVDC) transmissions [7]-[13], electric railway supplies [14], high-power motor drives [15]-[18], and transformerless static synchronous compensator (STATCOM) [19]-[23], due to its advantages of modularity, scalability, redundancy, and high efficiency. Either the half-bridge or the full-bridge MMC is chosen based on the special characteristics of the aforementioned applications. The half-bridge MMC has the advantage of less number of semiconductor switches, whereas the full-bridge MMC (FMMC) has the advantage of a very wide DC output voltage range, making it an ideal option as an ice-melting DC source. The FMMC converter can also be easily adapted to operate as a STATCOM in good weather, and therefore the equipment can be fully utilized. Moreover, very few studies have investigated the basic operation principles and down-scaled lab prototype [24]-[26]. The startup, control strategies, parameter design, and test of medium-voltage high-current MMC de-icer are not seen. Overall, in China, the main existing DC de-icers are stationary types that adopt SCRs to generate the DC ice-melting source. The main drawbacks of the SCR-based DC de-icer include bulky volume and high distortion currents. Meanwhile, other VSCs, such as half-bridge MMC (HMMC), only have a small ice-melting range. By contrast, the proposed FMMC-based DC de-icer can overcome these drawbacks very well. However, the relative startup, control methods, and large-capacity FMMC DC de-icer experimental test method were not presented and analyzed before. The present work mainly solves these problems and presents a real industrial-level large-capacity FMMC DC de-icer, which has not been presented before in any other papers as well.

This study focuses on the startup, control strategies, and experiment tests of a 10 kV 1.5 kA MMC mobile de-icer. The outline of this work is organized as follows. Principles of the operation, including circuit topology, operation principle, and operating range of the DC voltage, are described in Section II. This process is followed by startup strategies as described in Section III. The main control strategies are proposed in Section IV. Several tests of the MMC de-icer in different operating scenarios are presented in Section V. Some conclusions are drawn in Section VI.

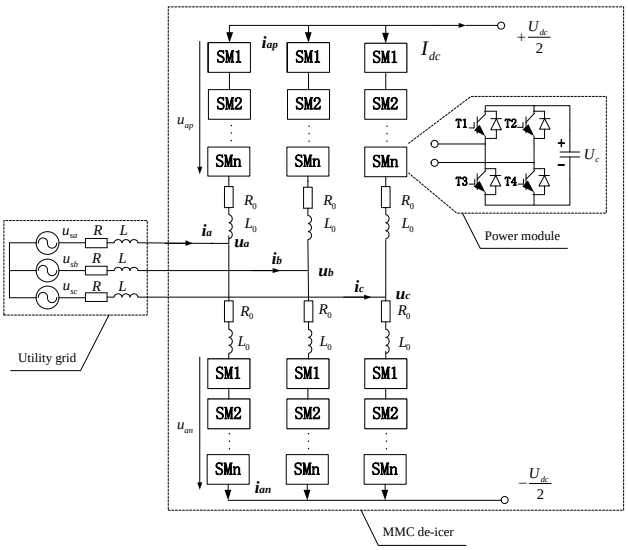

Fig. 1. Circuit topology of the mobile DC de-icer based on MMC.

II. Principle of Operation

A. Circuit Topology

Fig. 1 shows the topology of the MMC de-icer, which is composed of an MMC based on full-bridge sub-modules (SMs). The MMC has excellent scalability and outstanding output waveform quality; hence, the transformer and filter are no longer needed. As shown in Fig. 1, the three-phase FMMC is composed of six arms, each consisting of N series-connected full-bridge SMs and an arm inductor (L_0). The structure of a full-bridge SM is also shown in Fig. 1.

As shown in Fig. 1, u_{sa}, u_{sb}, and u_{sc} denote the three-phase voltages of the 10 kV AC power sources; u_{ap} and u_{an} denote the upper- and lower-arm voltages, respectively; i_{ap} and i_{an} denote the upper- and lower-arm currents, respectively; and I_{dc} denotes the DC current.

B. Operating Principle

One phase is taken as an example in the following sections because of the similarity of the three phases. According to Kirchhoff's voltage law, the following dynamic differential equations can be obtained. In the following sections, subscripts j, i, and x denote phases a, b, and c, and the number of SMs and upper or lower arm is denoted by p and n, respectively.

$$L_0\frac{di_{jp}}{dt}+R_0 i_{jp}=\frac{1}{2}U_{dc}-u_{jp}-u_{sj}+L\frac{di_j}{dt}+Ri_j\,. \tag{1}$$

$$L_0\frac{di_{jn}}{dt}+R_0 i_{jn}=\frac{1}{2}U_{dc}-u_{jn}+u_{sj}-L\frac{di_j}{dt}-Ri_j\,. \tag{2}$$

$$i_j=i_{jn}-i_{jp} \tag{3}$$

The following equations can be obtained by combining (1) with (3).

$$(L+\frac{L_0}{2})\frac{di_j}{dt}+(R+\frac{R_0}{2})i_j=u_{sj}-\frac{1}{2}(u_{jn}-u_{jp})\,. \tag{4}$$

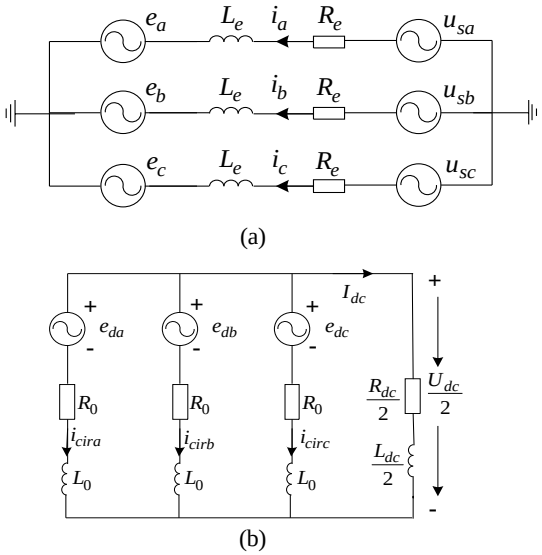

Fig. 2. Equivalent circuit of the MMC de-icer: (a) AC loop, (b) DC loop.

$$\frac{L_0}{2}\frac{d(i_{jp}+i_{jn})}{dt}+\frac{R_0}{2}(i_{jp}+i_{jn})=\frac{1}{2}U_{dc}-\frac{1}{2}(u_{jp}+u_{jn}). \quad (5)$$

We define the AC electromotive force (EMF) e_j, DC EMF e_{dj}, and arm circulating current i_{jcir} as

$$e_j=\frac{1}{2}(u_{jn}-u_{jp}). \quad (6)$$

$$e_{dj}=\frac{1}{2}(u_{jp}+u_{jn}). \quad (7)$$

$$i_{jcir}=\frac{1}{2}(i_{jp}+i_{jn}). \quad (8)$$

(4) and (5) can be rewritten as

$$L_e\frac{di_j}{dt}+R_e i_j=u_{sj}-e_j. \quad (9)$$

$$L_0\frac{di_{jcir}}{dt}+R_0 i_{jcir}=\frac{1}{2}U_{dc}-e_{dj}. \quad (10)$$

In (9) and (10), $L_e=L+\frac{1}{2}L_0$ and $R_e=R+\frac{1}{2}R_0$.

In the de-icing mode, the DC loop satisfies the following dynamic differential equation:

$$U_{dc}=L_{dc}\frac{dI_{dc}}{dt}+R_{dc}I_{dc}. \quad (11)$$

The AC and DC equivalent circuit models are illustrated in Figs. 2 (a) and (b). Accordingly, (9), (10), and (11) describe the mathematical models of the AC side, internal side, and DC side, respectively.

C. Operating Range of the DC Voltage

The wide range of the DC voltage is essential for a mobile FMMC de-icer because it will be used for different line lengths and conductor sizes. The operating range of the DC voltage is analyzed based on the following assumptions.

Assumption 1: SMs are identical, whereas voltage ripples are neglected.

Assumption 2: The switching function is replaced by an average function.

Therefore, the upper or lower arm can be regarded as a controllable voltage source, whose modulation functions are described as follows. One takes phase *a* as an example. The DC and AC modulation indexes are defined as $d=e_{da}/NU_d$ and $m=\hat{e}_a/NU_d$, respectively, where N and U_d denote the number of arm SMs and rated voltage of the SM capacitor, respectively. When the modulation indexes are used, the upper- and lower-arm modulation functions can be expressed as

$$\begin{cases}S_{ap}=d-m\sin(\omega t)\\ S_{an}=d+m\sin(\omega t)\end{cases}. \quad (12)$$

In (12), d and m denote the DC and AC modulation indexes, and S_{ap} and S_{an} denote the average modulation indexes of the upper and lower arms, respectively. The upper- and lower-arm voltages are expressed as

$$\begin{cases}u_{ap}=NU_d[d-m\sin(\omega t)]\\ u_{an}=NU_d[d+m\sin(\omega t)]\end{cases}, \quad (13)$$

where U_d denotes the SM DC voltage. Accordingly, the DC EMF and AC EMF are derived.

$$\begin{cases}e_{da}=dNU_d\\ e_a=mNU_d\sin(\omega t)\end{cases}. \quad (14)$$

The ratio between the DC voltage and the AC EMF r is expressed as

$$r=\frac{U_{dc}}{e_a}=\frac{2e_{da}}{e_a}=\frac{2d}{m}. \quad (15)$$

Generally, the half-bridge SM cannot generate a negative-voltage level, whereas the full-bridge SM can generate a negative-voltage level. Accordingly, the two topologies satisfy different constraints as follows:

(1) Full-bridge SM

$$\begin{cases}d+m\le 1\\ 0\le d\le 1\\ 0\le m\le 1\end{cases}. \quad (16)$$

Therefore, d and m must satisfy the following inequalities:

$$\begin{cases}0\le d\le 1-m\\ 0\le m\le 1\end{cases}. \quad (17)$$

(2) Half-bridge SM

$$\begin{cases}d+m\le 1\\ m\le d\le 1\\ 0\le m\le 1\end{cases}. \quad (18)$$

The following inequalities can be obtained by simplifying (18).

$$\begin{cases}m\le d\le 1-m\\ 0\le m\le 0.5\end{cases}. \quad (19)$$

Therefore, (17) and (19) are the constraints, which have to be satisfied by full-bridge SM and half-bridge SM, respectively. According to the constraints, the DC voltage

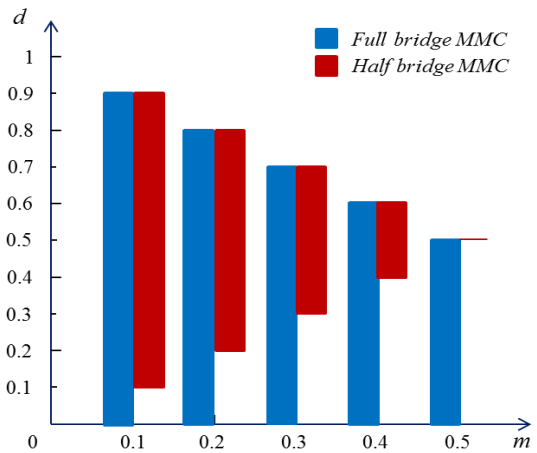

Fig. 3. Operating range of DC voltage modulation indexes of the FMMC and HMMCs.

(i.e., de-icing voltage) output ranges of FMMC and HMMC can be analyzed. One can obtain the following results by taking m=0.5 as an example and substituting m=0.5 into (17) and (19). In FMMC, $0 \le d \le 0.5$; in HMMC, $d = 0.5$. Then, one can obtain the following results by substituting the d values into (14). In FMMC, $0 \le e_{da} \le 0.5NU_d$; in HMMC, $e_{da} = 0.5NU_d$. Evidently, FMMC has a larger DC voltage output range than HMMC, which makes FMMC more suitable for mobile DC de-icing application. Different lengths and voltage levels of lines can be easily adapted with an FMMC de-icer. The overall comparison of DC voltage modulation indexes between the FMMC and HMMC is illustrated in Fig. 3, which clearly shows that FMMC is more suitable for the mobile de-icer application because of its wider DC voltage range compared with that of HMMC.

III. Startup Strategy

Several startup strategies of the MMC were introduced in [25], [26]. The key of the startup process is to charge all SM DC capacitors and minimize the impact on the AC system during the process. Startup strategies mainly have two kinds: the first one is charging SMs by auxiliary power source, in which an auxiliary power source is used to charge SMs one by one; and the second one is charging SMs by uncontrolled rectifier through the AC utility grid [27]. The auxiliary power source charging method is not a good option because of the increased complexity of the system. By contrast, the uncontrolled rectifier can only charge the DC capacitor voltage of the SM to a relatively low value. Therefore, it may cause a large inrush current at the instant of switching to an automatic control if the arm inductance is small. This incident may likewise result in over-voltage and over-current and even instability. Therefore, two charging methods by the utility grid are proposed to avoid these risks. Both methods contain two steps: (1) uncontrolled charging and (2) controlled charging.

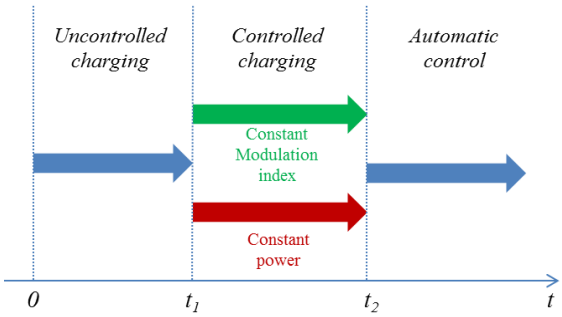

Fig. 4. Startup process of the proposed startup strategies.

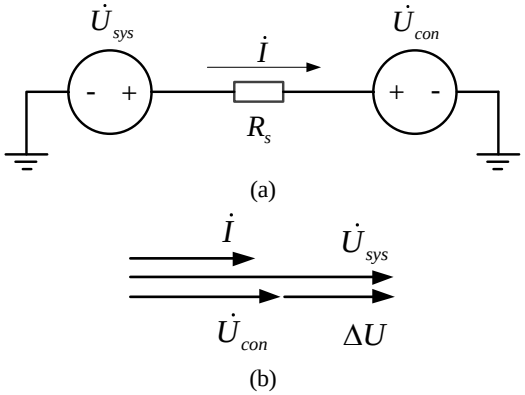

Fig. 5. Single-phase equivalent circuit and vector diagram.

Two objectives can be set in the controlled charging step. One objective is to set the modulation index constant, and the other is to ensure the constant charging power. The processes of the two methods are illustrated in Fig. 4. At the end of the controlled charging step, the startup resistor (Rs) is bypassed and the system is switched to automatic control.

The single-phase equivalent circuit of the controlled charging step is illustrated in Fig. 5 (a). $\dot{U}_{sys}$ denotes the line-to-neutral voltage of utility grid, $\dot{U}_{con}$ denotes the output voltage of one-phase SMs, and $\dot{I}$ and R_s denote the charging current and startup resistor, respectively. The resistance of R_s is large enough; hence, inductances and resistances of the system and arms can be neglected. Fig. 5 (b) shows the vector relationship of these variables during the charging process. During the first step, the drive signals to all the insulated-gate bipolar transistors (IGBTs) are blocked, and the full-bridge MMCs operate as diode rectifiers to charge the SM capacitors. The SM voltages are raised to $\sqrt{6}U_{sys}/2N$. The second steps are different between the two methods.

A. Constant Modulation Index Charging

The upper and lower arms are regarded as two independent controlled sources during the controlled charging step. Through the phase lock loop (PLL), the phase angle of the output AC voltage follows that of the utility grid, as shown in Fig. 5 (b). Therefore, the charging voltage and current can be expressed as follows.

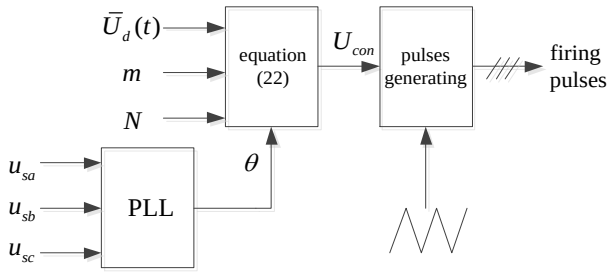

Fig. 6. Constant modulation index charging strategy.

$$\Delta\dot{U} = \dot{U}_{sys} - \dot{U}_{con} . \tag{20}$$

$$\dot{I} = \frac{\Delta\dot{U}}{R} . \tag{21}$$

The converter absorbs pure active power from the utility grid, and the SM DC voltage U_d keeps rising. The modulation index m is kept constant; hence, the amplitude of $\dot{U}_{con}$ keeps rising in proportion to U_d, and the charging current $\dot{I}$ tends to become zero. One realization is illustrated in Fig. 6.

(22) shows U_{con} generated by average voltage $\bar{U}_d(t)$, modulation index m, and SM number N.

$$U_{con} = \frac{mN\bar{U}_d(t)\sin(\theta)}{\sqrt{2}} . \tag{22}$$

The FMMC is composed of two identical cascaded H bridges, and the charging current of one H bridge is $I/2$. Therefore, the charging power of single-phase cascaded H bridges is expressed as

$$P = \frac{1}{2}U_{con}I = \frac{1}{2}\frac{mU_d}{\sqrt{2}}IN , \tag{23}$$

where $U_{con} = NmU_d/\sqrt{2}$ and U_d denotes the SM capacitor voltage. Through this charging method, the maximum U_d must satisfy the following equation:

$$NmU_d^{\max} = \sqrt{2}U_{sys} . \tag{24}$$

Then, the $U_d^{\max}$ can be derived as

$$U_d^{\max} = \frac{\sqrt{2}U_{sys}}{Nm} . \tag{25}$$

The charging power satisfies the following equation:

$$P = \frac{Nd(\frac{1}{2}CU_d^2)}{dt} = \frac{NmU_d}{\sqrt{2}} \bullet \frac{U_{sys} - \frac{mNU_d}{\sqrt{2}}}{2R_s} . \tag{26}$$

(26) can be rewritten as

$$\frac{dU_d}{dt} + \frac{k^2N}{2R_sC}U_d = \frac{k}{2R_sC}U_{sys} , \tag{27}$$

where k denotes $m/\sqrt{2}$.

The SM voltage during the charging procedure can be derived by solving (27).

$$U_d(t) = \frac{\sqrt{2}U_{sys}}{Nm} - [\frac{\sqrt{2}U_{sys}}{Nm} - U_d(0)]e^{-\frac{t}{\tau}}, \tau = \frac{4R_sC}{Nm^2} . \tag{28}$$

TABLE I
MAIN-CIRCUIT PARAMETERS OF 10 KV 1.5 KA MMC DE-ICER

U_{sys}	N	C	R_s	m
$10/\sqrt{3}$ kV	14	8.4 mF	5.1 kohm	0.9

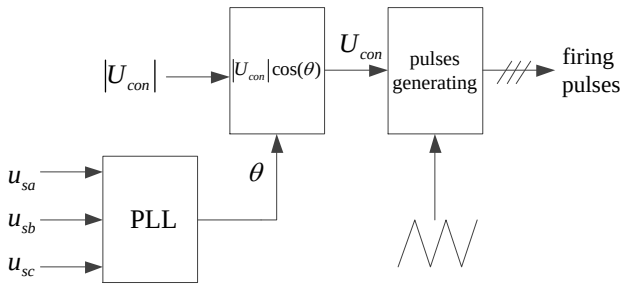

Fig. 7. Constant power charging strategy.

$U_d(0)$ is equal to the end value of the uncontrolled charging ($\sqrt{6}U_{sys}/2N$), and (29) can thus be derived from (28).

$$U_d(t) = \frac{\sqrt{2}U_{sys}}{N}[\frac{1}{m} - (\frac{1}{m} - \frac{\sqrt{3}}{2})e^{-\frac{t}{\tau}}] . \tag{29}$$

Here, we calculate the charging time based on a set of 10 kV 1.5 kA MMC de-icer parameters in Table I. These parameters will be discussed in the following section.

The time constant is equal to 15.2 s. Charging SM capacitors to $\sqrt{2}U_{sys}/N = 583$V takes 12.03 s.

B. Constant Power Charging

As shown in (22), the amplitude of U_{con} keeps rising with a constant modulation index m. Meanwhile, the charging current keeps decreasing until $\Delta\dot{U} = 0$. Another charging method is to control the output voltage of the converter a constant by adjusting the modulation index m^* according to (30). The block diagram of the constant power charging strategy is illustrated in Fig. 7.

The variable modulation index m^* is defined as

$$m^* = \frac{U_d^c}{U_d(t)} , \tag{30}$$

where $U_d^c \le U_d(0)$. If $U_d^c = U_d(0)$ is selected, then the modulation index m^* will continue to decrease from 1. Then, the SM output voltage remains $U_d(0)/\sqrt{2}$. The AC voltage of the utility grid remains constant, and thus the constant charging power of a single SM is expressed as

$$P_0 = \frac{U_d(0)}{\sqrt{2}}\frac{I}{2} . \tag{31}$$

The charging power satisfies the following equation.

$$\frac{d(\frac{1}{2}CU_d^2)}{dt} = P_0 . \tag{32}$$

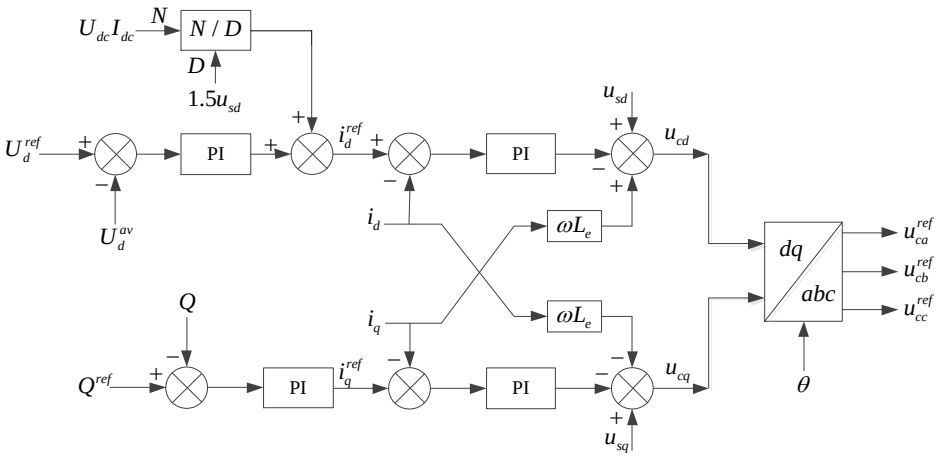

Fig. 8. Average voltage of all SMs and reactive power control.

Then, by solving (32), U_d can be expressed as follows.

$$U_d^2(t) = U_d^2(0) + \frac{2P_0}{C}t\,. \tag{33}$$

In addition, by using the parameters in Table I, (33) will turn to

$$U_d^2(t) = 505^2 + \frac{2\times 27.1}{8.4}\times 10^3 t\,. \tag{34}$$

Charging SM capacitors to 583 V by the constant power charging method takes 13.16 s. Unlike the constant modulation index method, this constant power charging method can charge the SM voltage as high as needed theoretically. Therefore, this constant power charging method is a good option. $U_d(0)$ is determined by the utility grid voltage. Thus, the charging time can be reduced by increasing the charging power P_0. The expression of a single SM power P_0 can be derived from (26).

$$P_0 = \frac{U_{sys}U_d}{2\sqrt{2}R_s}m - \frac{NU_d^2}{4R_s}m^2\,. \tag{35}$$

$$\frac{dP_0}{dm} = \frac{U_{sys}U_d}{2\sqrt{2}R_s} - \frac{NU_d^2}{2R_s}m\,. \tag{36}$$

By letting (36) be zero, we can derive m_0 as follows:

$$m_0 = \frac{U_{sys}}{\sqrt{2}NU_d}\,. \tag{37}$$

When $m = m_0$, P_0 acquires the maximum value and the charging time becomes the shortest. The shortest charging time t_{min} can be derived as follows:

$$P_0^{\max} = \frac{U_{sys}^2}{8NR_s}\,. \tag{38}$$

$$t_{\min} = \frac{4CNR_s}{U_{sys}^2}\left[U_d^2(t) - U_d^2(0)\right]. \tag{39}$$

By substituting parameters presented in Table I to (39), we can obtain the minimum charging time $t_{\min} = 6s$ when charging SM capacitors to 583 V.

IV. Main Control Strategy

This section proposes the main control strategies for the MMC de-icer. The main controller contains the following parts: (1) control of the average DC voltage of all SMs and reactive power, (2) control of de-icing current and average DC voltage of the SMs within each phase, (3) individual SM DC voltage control, and (4) PSC-PWM modulation.

A. Control of the Average Voltage of All SMs and Reactive Power

The traditional d–q decoupling current control is adopted to realize the regulation of average voltage of all SMs and reactive power control, as shown in Fig. 8, where θ denotes the synchronous phase angle of the utility grid generated by PLL. The active current reference i_d^{ref} is generated by the conjunction between the average voltage control and the AC/DC power-balance constraint. In the de-icing mode, the reactive power is controlled to zero. In the STATCOM mode, the reactive power command Q^{ref} is set as needed. In this block diagram, the U_d^{av} is given by

$$U_d^{av} = \frac{1}{6N}\sum_{j=a,b,c}\sum_{x=p,n}\sum_{i=1}^{N}U_{djxi}\,, \tag{40}$$

where U_d^{av} denotes the average voltage of all SMs. This control generates the AC voltage commands of the MMC. The inclusion of the DC power in the i_d^{ref} loop increases the system response.

B. Control of De-Icing Current and Average Voltage within each Phase

To avoid overcurrent during the de-icing process, the de-icing current rather than voltage is chosen as the command. As shown in Fig. 9, the command of circulating current of phase j is set to $I_{dc}^{ref}/3$, because the DC current is composed

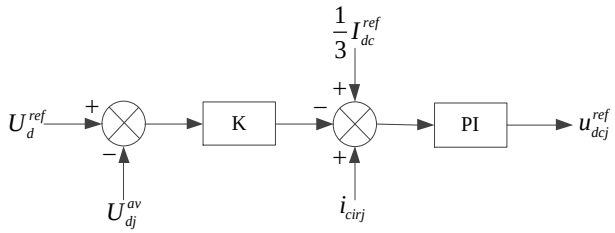

Fig. 9. De-icing current and phase average voltage control.

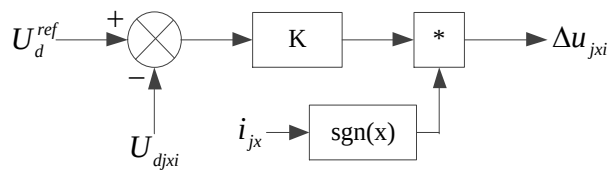

Fig. 10. Individual SM voltage control.

of three-phase circulating currents. The average SM voltage of phase j is also regulated by a proportional control added to the circulating current control loop. On a special note, the PI controller used here is for simplicity. The de-icing current and average voltage control of each phase generate the DC voltage command of the MMC. In the STATCOM mode, I_{dc}^{ref} is set to zero and the average voltage of phase j U_{dj}^{av} is given by

$$U_{dj}^{av} = \frac{1}{2N}\sum_{x=p,n}\sum_{i=1}^{N} U_{djxi} \,. \tag{41}$$

C. Individual SM Voltage Control

The average voltage of SMs is regulated by the aforementioned controllers. As a result, the individual SM also should be controlled to follow its command U_d^{ref}, as shown in Fig. 10. The individual SM voltage control is based on the polarity of arm currents. Function sgn(x) represents 1, if x>0; 0, if x=0; −1, if x<0. The SM capacitor absorbs energies when capacitor voltage is lower than its command and release energies when capacitor voltage is higher than its command. This individual SM voltage control generates an additional voltage Δu_{jxi}.

D. PSC-PWM Modulation

According to the operation principles of MMCs, the voltage command of individual SM is expressed in the following equations:

$$\begin{cases} u_{jpi} = \dfrac{1}{N}(u_{dcj}^{ref} - u_{cj}^{ref} + \Delta u_{jpi}) \\ u_{jni} = \dfrac{1}{N}(u_{dcj}^{ref} + u_{cj}^{ref} + \Delta u_{jni}) \end{cases}. \tag{42}$$

Shifted phase angles of the upper and lower arms are π/N. The firing pulses are generated by the PSC-PWM method, as shown in Fig. 11.

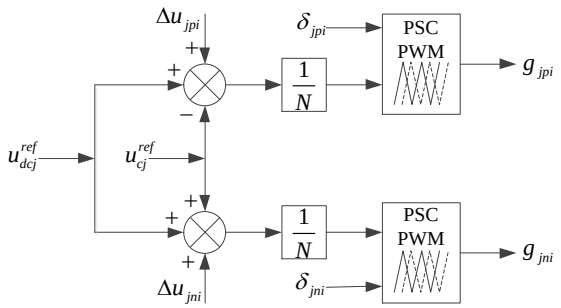

Fig. 11. PSC-PWM modulation block diagram.

TABLE II
MAIN-CIRCUIT PARAMETERS FOR THE MMC DE-ICER

Items	Symbols	Values
Rated AC bus line-to-line voltage	u_s	10 kV
Rated frequency	f	50 Hz
Carrier frequency	f_s	300 Hz
Rated direct current	I_{dc}	1.5 kA
Rated direct voltage	U_{dc}	6 kV
Arm inductance	L_0	2.4 mH
Number of SMs per arm	N	14
Rated capacitor voltage	U_d	900 V
Capacitor capacitance	C	8400 uF

V. EXPERIMENTAL STUDY

The 10 kV 1.5 kA mobile MMC de-icer is illustrated in Fig. 12. Parameters of the MMC de-icer are shown in Table II. To reduce losses and experimental conditions, a novel rated-current zero-power experiment scheme is proposed. As analyzed before, a maximum value of capacitor voltage ripple is present under the rated-current zero-power condition. An inductor with small inductance L_{dc} is connected to the DC side, which represents the DC line, as shown in Fig. 13. Four cases are tested.

To clearly express the experimental results, graphic symbols are introduced in the following pictures. The vertical axis represents the voltage or current, whose units are kV or kA, respectively. The horizontal axis represents time with display format of "hour: minute: second. millisecond, date/month/year."

A. Case 1: Startup Scenario

Fig. 14 depicts the SM average voltages during the startup process, which verifies the proposed startup strategy. Constant power startup method is adopted in this test. The durations of the uncontrolled charge, controlled charge, and automatic control are labeled in Fig. 16, where three time instants (*a*, *b*, *c*) are labeled. At instant *a*, startup begins and the de-icer starts uncontrolled charging. Then, the capacitor voltage reaches approximately 460 V, which is a little less than the analytical value of 505 V, because the analysis ignores the voltage drop of the starting resistor. At instant *b*,

(a)

(b)

(c)

Fig. 12. Photographs of the 10 kV 1.5 kA mobile MMC de-icer. (a) Appearance of the whole system. (b) A section of the SM bank. (c) Single power module.

startup progress switches to controlled charge process. Finally, at instant *c*, automatic control is switched in to raise the capacitor voltage to the rated value quickly. The startup method is valid and one can switch from controlled charge to the automatic control before the SM voltages reach rated values.

Fig. 15 illustrates arm currents during the startup process. Evidently, some inrush currents are present at instant *c* when switching from controlled charge to automatic control. As shown in the figure, the amplitudes of the inrush currents are less than 90 A.

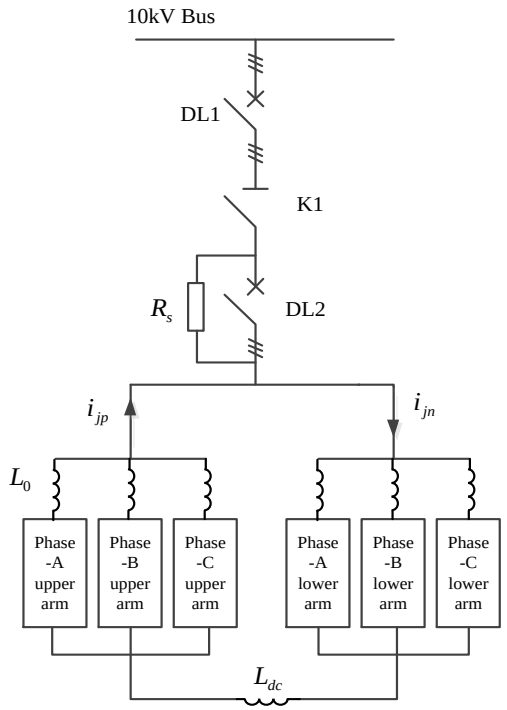

Fig. 13. Electrical diagram of zero-power experiment scheme.

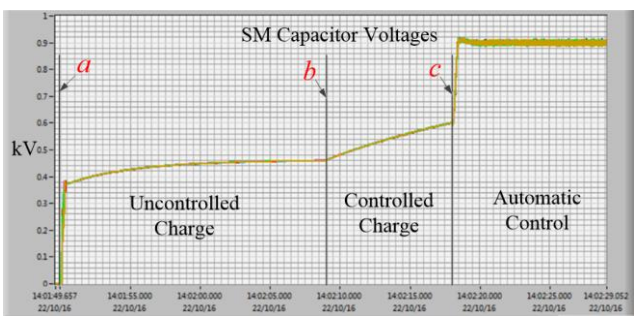

Fig. 14. SM average voltages during the startup procedure.

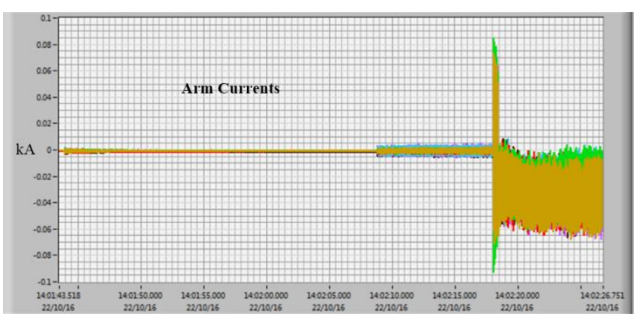

Fig. 15. Arm currents during the startup process.

B. Case 2: Rated-Current Zero-Power Test

Rated-current zero-power test is a novel test on the 10 kV 1.5 kA MMC de-icer for energy conservation. It uses an inductor instead of a real overhead transmission line, which is not easy to obtain. Given that the DC current flows through the inductor, the loss is few and it can be neglected. Parts of

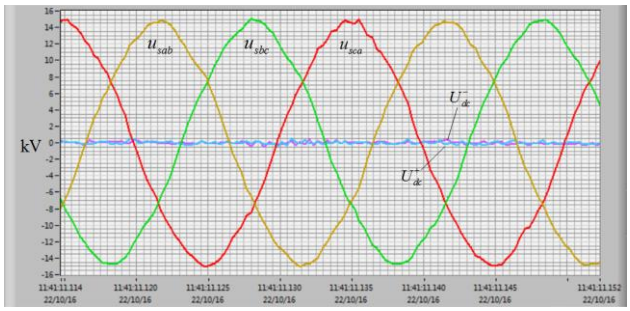

Fig. 16. Line-to-line voltages of the utility grid.

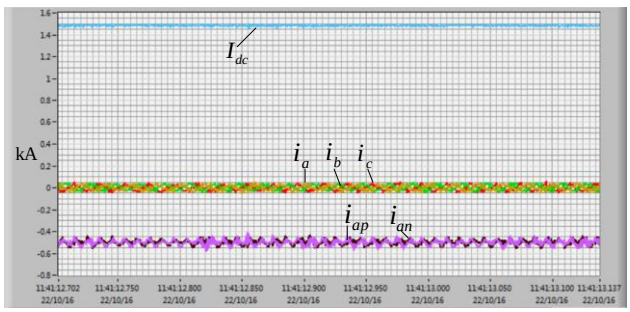

Fig. 17. Dc, AC, and arm currents on rated ice-melting current zero-power condition.

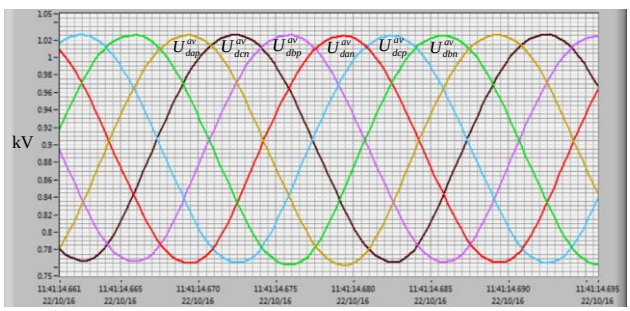

Fig. 18. SM average voltages of six arms on rated ice-melting current zero-power condition.

the waveforms are illustrated in Figs. 16 to 18, where DC voltage is near zero, while the utility grid voltages have non-negligible harmonics, as shown in Fig. 16. Fig. 17 depicts that I_{dc} follows its command 1.5 kA, AC currents are near zero, and arm currents of phase *a* are 500 A with some ripples. Fig. 18 illustrates the SM average voltages of six arms. Based on the experimental results, the rated-current zero-power test has rated DC current (1.5 kA) but almost zero AC current (Fig. 17). This result means that the control method proposed in Section IV can work well under extremely small AC current, which demonstrates that the control method has good robustness.

C. Case 3: STATCOM Operation Test

A test of two STATCOMs (upper arms and low arms) exchanging reactive power is carried out. A 500 A reactive current is set as a command. The upper-arm STATCOM transfers reactive power to the lower-arm STATCOM. Figs. 19 and 20 depict the arm currents and SM average voltages during this test. The reactive currents have good waveform quality with little distortion, and the capacitor voltages in all arms are balanced very well.

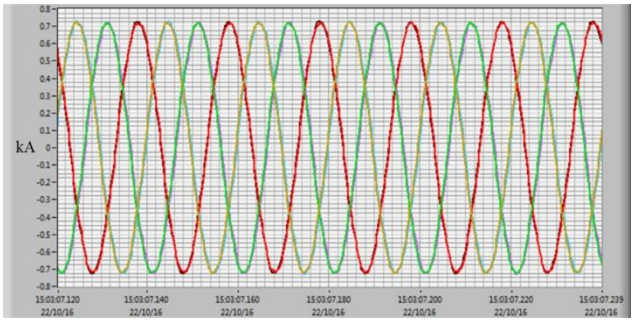

Fig. 19. SM average voltages of six arms on rated ice-melting current zero-power condition.

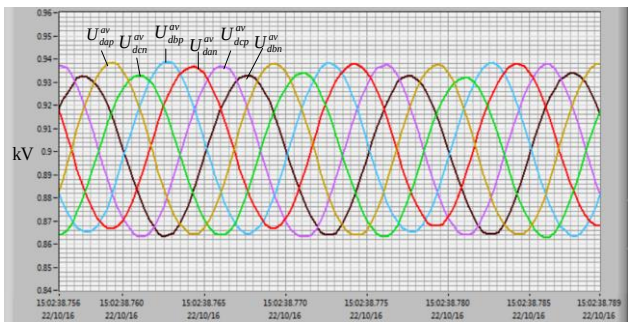

Fig. 20. SM average voltages of six arms on rated STATCOM condition.

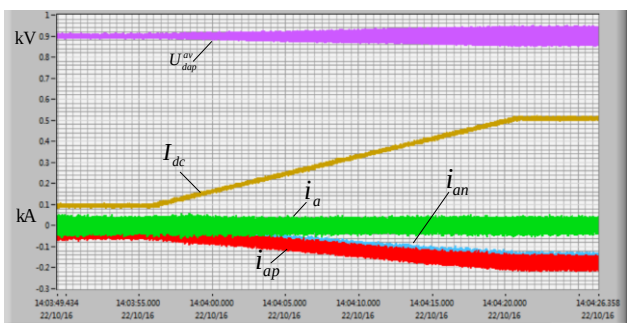

Fig. 21. Currents and SM average voltage of phase-*a* on the de-icing transient condition.

D. Case 4: Transient-State Operation

To verify the transient characteristics of the proposed control method, a transient experiment in which DC current command is set a ramp change from 0.1 kA to 0.5 kA is conducted. The transient-state experiment results on the rated-current zero-power de-icing condition are illustrated in Fig. 21. Clearly, the DC current (I_{dc}) follows the ramp command very well without overcurrent, arm currents (i_{ap}, i_{an}) change smoothly correspondingly, the ripple of upper-arm capacitor average voltage of phase-*a* becomes large correspondingly, and the AC current of phase-*a* remains stable.

VI. CONCLUSION

This work introduces an FMMC mobile DC de-icer with STATCOM function. The main control strategies and two novel controlled startup strategies are proposed for this MMC de-icer. A new rated-current zero-power test of the prototype is proposed to simplify the test conditions. Finally, the proposed startup and control strategies are verified by some experiments on a 10 kV 1.5 kA MMC de-icer.

REFERENCES

[1] C. Horwill, C. C. Davidson, and M. Granger, "An application of HVDC to the de-icing of Transmission Lines," *2005/2006 IEEE/PES Transmission and Distribution Conference and Exhibition*, pp. 529-534, 2006.

[2] J. Wang, C. Fu, Y. Chen, H. Rao, S. Xu, T. Yu, and L. Li, "Research and application of DC de-icing technology in china southern power grid," *IEEE Trans. Power Del.*, Vol. 27, No. 3, pp. 1234-1242, Jul. 2012.

[3] S. Li, Y. Wang, X. Li, W. Wei, G. Zhao, and P. He, "Review of de-icing methods for transmission lines," in *Proc. Int. Conf. Intel. Syst. Design Eng. Appl.*, Vol. 2, pp. 310-313, 2010.

[4] C. Volat, M. Farzaneh, and A. Leblond, "De-icing/ anti-icing techniques for power lines: Current methods and future direction," in *Proc. 11th Int. Workshop Atmos. Icing Structure*, pp. 1-11, 2005.

[5] Y. Chen, Q. Wang, B. Gu, Y. Cai, and F. Wen, "Research on the operating process of DC de-icer and its de-icing efficiency in china southern power grid," *2012 Conference on Power & Energy - IPEC*, pp. 583-588, 2012.

[6] C. Wang, J. Wen, S. Li, X. Ma, and J. Wang, "Design on DC de-icing schemes for high voltage transmission line," in *Proc. 5th Critical Infrastructure Int. Conf.*, pp. 1-5, Sep. 2010.

[7] P. Hu, D. Jiang, Y. Zhou, Y. Liang, J. Guo, and Z. Lin, "Energy-balancing control strategy for modular multilevel converters under submodule fault conditions," *IEEE Trans. Power Electron.*, Vol. 29, No. 9, pp. 5021-5030, Sep. 2014.

[8] P. Hu and D. Jiang, "A level-increased nearest level modulation method for modular multilevel converters," *IEEE Trans. Power Electron.*, Vol. 30, No. 4, pp. 1836-1842, Apr. 2015.

[9] Y. Zhou, D. Jiang, P. Hu, J. Guo, Y. Liang, and Z. Lin, "A prototype of modular multilevel converters," *IEEE Trans. Power Electron.*, Vol. 29, No. 7, pp. 3267-3278, Jul. 2014.

[10] A. Hassanpoor, A. Nami, and S. Norrga, "Tolerance band adaptation method for dynamic operation of grid-connected modular multilevel converters," *IEEE Trans. Power Electron.*, Vol. 31, No. 12, pp. 8172-8181, Dec. 2016.

[11] J. Guo, D. Jiang, Y. Zhou, P. Hu, Z. Lin, and Y. Liang, "Energy storable VSC-HVDC system based on modular multilevel converter," *International Journal of Electrical Power & Energy Systems*, Vol. 78, pp. 269-276, Jun. 2016.

[12] S. Cui and S. Sul, "A comprehensive DC short-circuit fault ride through strategy of hybrid modular multilevel converters (MMCs) for overhead line transmission," *IEEE Trans. Power Electron.*, Vol. 31, No. 11, pp. 7780-7796, Nov. 2016.

[13] J. Xu, P. Zhao, and C. Zhao, "Reliability analysis and redundancy configuration of mmc with hybrid submodule topologies," *IEEE Trans. Power Electron.*, Vol. 31, No. 4, pp. 2720-2729, Apr. 2016.

[14] M. Glinka, and R. Marquardt, "A new AC/AC multilevel converter family," *IEEE Trans. Ind. Electron.*, Vol. 52, No. 3, pp. 662-669, Jun. 2005.

[15] A. Antonopoulos, K. Ilves, L. Ängquist, and H. P. Nee, "On interaction between internal converter dynamics and current control of high-performance high-power AC motor drives with modular multilevel converters," *2010 IEEE Energy Conversion Congress and Exposition*, pp. 4293-4298, 2010.

[16] M. Hagiwara, K. Nishimura, and H. Akagi, "A medium-voltage motor drive with a modular multilevel PWM inverter," *IEEE Trans. Power Electron.*, Vol. 25, No. 7, pp. 1786-1799, Jul. 2010.

[17] A. J. Korn, M. Winkelnkemper, and P. Steimer. "Low output frequency operation of the Modular Multi-Level Converter", in *2010 IEEE Energy Conversion Congress and Exposition*, pp. 3993-3997, 2010.

[18] A. Antonopoulos, L. Ängquist, S. Norrga, K. Ilves and H. P. Nee, "Modular multilevel converter ac motor drives with constant torque form zero to nominal speed," *2012 IEEE Energy Conversion Congress and Exposition (ECCE)*, pp. 739-746, 2012.

[19] Y. Liang and C. O. Nwankpa, "A new type of STATCOM based on cascading voltage-source inverters with phase-shifted unipolar SPWM," *IEEE Trans. Ind. Appl.*, Vol. 35, No. 5, pp. 1118-1123, Sep./Oct. 1999.

[20] G. P. A. Miet, O. A. L. Mieee, G. B. Mieee, and J. M. Smieee, "Transformerless STATCOM based on a five-level modular multilevel converter," *2009 13th European Conference on Power Electronics and Applications*, pp. 1-10, 2009.

[21] M. Hagiwara, R. Maeda, and H. Akagi, "Negative-sequence reactive-power control by a PWM STATCOM based on a modular multilevel cascade converter (MMCC-SDBC)," *IEEE Trans. Ind. Appl.*, Vol. 48, No. 2, pp. 720-729, Mar./ Apr. 2012.

[22] X. Yu, Y. Wei, and Q. Jiang, "STATCOM operation scheme of the CDSM-MMC during a pole-to-pole DC fault," *IEEE Trans. Power Del.*, Vol. 31, No. 3, pp. 1150-1159, Jun. 2016.

[23] G. Tsolaridis, H. A. Pereira, A. F. Cupertino, R. Teodorescu and M. Bongiorno, "Losses and cost comparison of DS-HB and SD-FB MMC based large utility grade STATCOM," *2016 IEEE 16th International Conference on Environment and Electrical Engineering (EEEIC)*, pp. 1-6, 2016.

[24] Y. Guo, J. Xu, C. Guo, C. Zhao, C. Fu, Y. Zhou, and S. Xu, "Control of full-bridge modular multilevel converter for dc ice-melting application," *11th IET International Conference on AC and DC Power Transmission*, pp. 1-8, 2015.

[25] H. Mei and J. Liu, "A novel dc ice-melting equipment based on modular multilevel cascade converter," *Autom. Elect. Power Syst.*, Vol. 37, No. 16, pp. 96-102, Aug. 2013. (in Chinese)

[26] B. Li, S. Shi, D. Xu, and W. Wang, "Control and analysis of the modular multilevel DC de-icer with STATCOM functionality," *IEEE Trans. Ind. Electron.*, Vol. 63, No. 9, pp. 5465-5476, Sep. 2016.

[27] J. Qin, S. Debnath and M. Saeedifard, "Precharging strategy for soft startup process of modular multilevel converters based on various SM circuits," *2016 IEEE Applied Power Electronics Conference and Exposition (APEC)*, pp. 1528-1533, 2016.
[28] Q. Yeniu, W. Jianbo, D. C. Jun, and S. Jian, "Research on the pre-charging control strategies of the series part of MMC-UPQC," *2016 IEEE 11th Conference on Industrial Electronics and Applications (ICIEA)*, pp. 474-478, 2016.
[29] B. Li, D. Xu, Y. Zhang, R. Yang, G. Wang, W. Wang, and D. Xu, "Closed-loop precharge control of modular multilevel converters during start-up processes," *IEEE Trans. Power Electron.*, Vol. 30, No. 2, pp. 524-531, Feb. 2015.
[30] Y. Zhou, D. Jiang, J. Guo, P. Hu and Y. Liang, "Analysis and control of modular multilevel converters under unbalanced conditions," *IEEE Trans. Power Del.*, Vol. 28, No. 4, pp. 1986-1995, Oct. 2013.
[31] Z. Xu, H. Xiao, and Z. Zhang, "Selection methods of main circuit parameters for modular multilevel converters," in *IET Renewable Power Generation*, Vol. 10, No. 6, pp. 788-797, Jul. 2016.

Pengfei Hu was born in Suining, China, on January 8, 1988. He received his B.E. and Ph.D. degrees in Electrical Engineering and Its Automation from the College of Electrical Engineering, Zhejiang University, Hangzhou, China, in 2010 and 2015, respectively. He is now working as an assistant professor in the University of Electronic Science and Technology of China. His research interests include high-voltage DC transmission, flexible AC transmission systems, and DC distribution network.

Yiqiao Liang received his B.S. and M.S. degrees in Electrical Engineering from Zhejiang University, Hangzhou, China, in 1984 and 1987, respectively, and his Ph.D. degree in Electrical Engineering from Drexel University, Philadelphia, PA, in 2000. He is currently a research fellow with the College of Electrical Engineering, Zhejiang University. His research interests are in the fields of power electronics and power systems.

Yi Du was born in Fujian, China, on January 19, 1990. He received his B.E. and M.S. degrees in Electrical Engineering and Its Automation from the College of Electrical Engineering, Zhejiang University, Hangzhou, China, in 2012 and 2015, respectively. He is currently working as an engineer in State Grid Fujian Electric Power Co., Ltd. His research interests include energy economy and high-voltage DC transmission.

Renming Bi was born in Wuhu, China, on November 25, 1977. He received his B.E. and M.S. degrees in Electrical Engineering and Its Automation from the College of Electrical Engineering, Xi'an Jiaotong University, Xi'an, China, in 2000 and 2008, respectively. He is now working as an electrical engineer in Zhejiang Guirong Xieping Technology Co., Ltd. His research interests include static VAR compensator, static VAR generator, high-voltage dc transmission, and flexible ac transmission systems.

Chonglin Rao was born in Daye, China, on September 25, 1976. He received his M.S. degree in Control Theory and Control Engineering from the Automation College, Wuhan University of Technology, Wuhan, China, in 2003. He is now working as an electrical engineer in Zhejiang Guirong Xieping Technology Co., Ltd. His research interests include thyristor switched capacitor, active power filter, and static VAR generator.

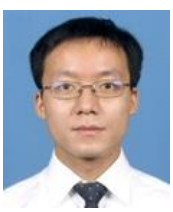

Yang Han (S'08-M'10-SM'17) received his Ph.D. in Electrical Engineering from Shanghai Jiao Tong University, Shanghai, China, in 2010. He joined the Department of Power Electronics, School of Mechatronics Engineering, University of Electronic Science and Technology of China in 2010 and has been an Associate Professor since 2013. From March 2014 to March 2015, he was a visiting scholar (guest postdoc) at the Department of Energy Technology, Aalborg University, Aalborg, Denmark. His research interests include AC/DC microgrids, grid-connected converters for renewable energy systems and DGs, power quality, active power filters, and static synchronous compensators. He has served as the Session Chair in "Power Quality Mitigation and Application" in the 5th National Conference on Power Quality in Xi'an in 2017 and the Session Chair in "AC/DC, DC/AC Power Converter" session in the 2016 IPEMC ECCE-Asia in Hefei, China. He was awarded "Baekhyun Award" by the Korean Institute of Power Electronics in 2016. He received the Best Paper Award from the 5th National Conference on Power Quality in 2017, the Annual Conference of HVDC and Power Electronics Committee of Chinese Society of Electrical Engineers in 2013, and the 4th International Conference on Power Quality in 2008, China.